Computers in Biology and Medicine 179 (2024) 108891

Contents lists available at ScienceDirect

Computers in Biology and Medicine

journal homepage: www.elsevier.com/locate/compbiomed

# Automatic identification of radius and ulna bone landmarks on 3D virtual models

Derek F.R. van Loon [a,*], Eline M. van Es [a], Denise Eygendaal [a], DirkJan H.E.J. Veeger [b], Joost W. Colaris [a]

[a] Department of Orthopaedics and Sports Medicine, Erasmus MC, University Medical Center Rotterdam, Dr. Molewaterplein 40, Rotterdam, 3015 GD, The Netherlands

[b] Department of Biomechanical Engineering, Delft University of Technology, Mekelweg 2, Delft, 2628 CD, The Netherlands

ARTICLE INFO

*Keywords:*
Forearm landmark detection
Knowledge-based
Automatic method
Computer-assisted orthopedic surgery (CAOS)

ABSTRACT

**Background:** For bone morphology and biomechanics analysis, landmarks are essential to define position, orientation, and shape. These landmarks define bone and joint coordinate systems and are widely used in these research fields. Currently, no method is known for automatically identifying landmarks on virtual 3D bone models of the radius and ulna. This paper proposes a knowledge-based method for locating landmarks and calculating a coordinate system for the radius, ulna, and combined forearm bones, which is essential for measuring forearm function. This method does not rely on pre-labeled data.
**Validation:** The algorithm is validated by comparing the landmarks placed by the algorithm with the mean position of landmarks placed by a group of experts on cadaveric specimens regarding distance and orientation.
**Results:** The median Euclidean distance differences between all the automated and reference landmarks range from 0.4 to 1.8 millimeters. The median angular differences of the coordinate system of the radius and ulna range from -1.4 to 0.6 degrees. The forearm coordinate system's median errors range from -0.2 to 2.0 degrees. The median error in calculating the rotational position of the radius relative to the ulna is 1.8 degrees.
**Conclusion:** The automatic method's applicability depends on the use context and desired accuracy. However, the current method is a validated first step in the automatic analysis of the three-dimensional forearm anatomy.

## 1. Introduction

The use of three-dimensional (3D) bone surface models is a new development in orthopedics [1]. These models are created by segmenting bones from computed tomography (CT) or magnetic resonance (MR) scans [2]. A virtual or printed 3D model improves the interpretation and analysis of patient-specific anatomy [3]. An example can be found in planning osteotomies to restore bone shapes. Research has shown that the use of 3D pre-operative planning improves outcomes over 2D planning [4].

One of the first steps in 3D pre-operative planning is calculating a coordinate system that defines the bone's general shape, position, and orientation. These coordinate systems are based on anatomical landmarks [5]. Manual annotation of these landmarks has high variability, which can be improved with automatic placement [6,7]. Automated placement algorithms can be, among other things, based on statistical shape or artificial intelligence. Still, these models require substantial computational power and a substantial amount of manually annotated data [8,9]. Algorithms based on a geometric approach do not have these drawbacks and have already been shown to be helpful in research and clinical use [10,11]. However, these methods are only reported for the lower extremity, skull, and humerus [10–14]. For the radius and ulna, no method is available at the moment.

This article describes a knowledge-based method for detecting anatomical landmarks on the radius and ulna. To evaluate this method, the automated method's landmarks are compared to those placed by experienced researchers working with 3D forearm models. The comparison is made for the location of the landmarks and the coordinate systems, which can be calculated from these landmarks for the radius, ulna, and forearm.

### 1.1. Related work

Techniques that provide a 3D virtual bone model with landmark locations as output have been published before. These studies can be divided into three types: knowledge-based, template-based, and learning-based.

* Corresponding author.
*E-mail address:* d.vanloon@erasmusmc.nl (D.F.R van Loon).

https://doi.org/10.1016/j.compbiomed.2024.108891
Received 1 March 2024; Received in revised form 12 July 2024; Accepted 12 July 2024
Available online 23 July 2024

Knowledge-based techniques use local shape information and features to identify edges, sharp points, valleys, and more on a surface. A shape feature can place a landmark based on orientation and location. Negrillo et al. described a method to find landmarks on the femur and humerus compared to a phantom [11,13]. In line with this study, Idram et al. used a knowledge-based method to find landmarks on calcaneus models to perform morphological measurements [15]. Thereby, Subburaj et al. used a curvature-based method to identify knee landmarks [6] and Fischer et al. describe a method for finding landmarks on the pelvic bone [10].

Template-based techniques create one template based on input data as a reference to fit a target of unseen data. The template is often calculated using an atlas or a statistical shape model. The simplest method is creating an atlas based on one or multiple labeled surfaces. Phan et al. used one labeled femur as a template for registration to place landmarks on another surface model [16]. Schroder et al. used multiple input surfaces for the femur, which led to a higher accuracy [17]. Because this technique depends on pre-labeled data and performs better when more data is available, Bermejo et al. first performed a template-based initialization of the landmarks, which was then improved with a knowledge-based step to find landmarks of the skull [18]. Fischer et al. used a hybrid model consisting of an atlas registration first, followed by a knowledge-based refinement, directly on 3D bone models of the femur [12].

Another way to create a template based on multiple bone models is using statistical shape modeling. This technique calculates a mean shape based on multiple input shapes. A new bone model is then transformed into the mean shape, and a back transformation places the landmarks. Baek et al. found 14 landmarks on a femur using statistical shape modeling [14]. Montúfar et al. use a hybrid model using two 2D orthogonal images created from a 3D model [19]. Both the anterior and lateral images are used as input for a shape model to calculate an initial placement of landmarks, which is further refined using a knowledge-based method.

Learning-based techniques use pre-labeled data to place labels or landmarks on new, unseen data without creating a template. These techniques are relatively new and based on different forms of artificial intelligence. A meta-analysis from Serafin et al. showed that the accuracy for 3D cephalometric landmark placement using deep learning algorithms is increasing in more recent research [20]. For example, Liu et al. found seven landmarks on patellofemoral CT scans using a deep-learning model [21].

By comparing the method section of these studies, the differences between the three methods and their advantages and disadvantages become apparent. While all methods reach an acceptable accuracy, the template and learning-based methods show better generalizability and adjustability than the knowledge-based methods. These are based on one principle, either surface registration, statistical shape modeling, or convolutional neural networks, and apply these to the anatomy of interest. A different anatomy often only requires adjusting parameters; however, the developer needs a comprehensive understanding of the underlying model for troubleshooting and implementation. On the contrary, the knowledge-based methods have a lower complexity and can be developed from a smaller, unlabeled dataset. These methods can use the same approaches, for example, finding the highest point or the center of a region of interest, but these all depend on the context of the bone and the landmarks of interest. A new bone requires, therefore, a new method.

Most of these studies used the lower extremity or skull as the anatomical subject. Similar research for the upper extremity is sparse. Only the knowledge-based method of Negrillio et al. places landmarks on the humerus [11]. No method has been published for the forearm focusing on the entire forearm or the proximal or distal radioulnar joint. Therefore, a knowledge-based method is a simple first step into automatically analyzing the forearm in 3D without the need for large amounts of pre-labeled data and an understanding of advanced techniques.

**Table 1**
Table describing the directions of the coordinate systems mentioned in this paper for a right-sided forearm.

| Axis | Displacement | | Rotation | |
|---|---|---|---|---|
| | + | − | + | − |
| *x* | Dorsal | Volar | Radial deviation | Ulnar deviation |
| *y* | Distal | Proximal | Supination | Pronation |
| *z* | Radial/lateral | Ulnar/medial | Flexion | Extension |

## 2. Method

### 2.1. Radial, ulnar, and forearm coordinate systems

An overview of the bony landmarks of interest is given in Fig. 1. The coordinate systems calculated in this study are primarily based on the recommendation of the International Society of Biomechanics (ISB) [5]. However, the coordinate system of the ulna is altered because it depends on bony structures of the radius and the position of the radius relative to the ulna. The aim is to calculate a coordinate system of the isolated ulna. The coordinate system of the forearm is changed because it depends on the bony structures of the humerus. The aim is to also calculate the rotational position of the radius relative to the ulna if the humerus is not available. The radial coordinate system is defined as follows. The *y*-axis is the line from the center of the radial head to the center of the ridge between the radioscaphoid and radiolunate fossae. The *z*-axis is the line from the base of the concavity of the ulnar notch to the radial styloid perpendicular to the *y*-axis. The *x*-axis is the common line perpendicular to the *y*-axis and *z*-axis. The ulnar coordinate system is defined as follows. The *y*-axis is the line from the proximal center to the ulnar fovea. The *x*-axis is the line from the ulnar styloid to the ulnar dome. The *z*-axis is the common line perpendicular to the *y*-axis and *x*-axis.

The coordinate system of the forearm is as follows. The *y*-axis is the line from the center of the radial head to the ulnar fovea, coincident with the rotation axis of the forearm [22]. The *x*-axis is the normal of the fitted plane through the radial head, trochlear notch, and ulnar fovea pointing volar. The *z*-axis is the common line perpendicular to the *y*-axis, and the *x*-axis points in the lateral direction. To measure the position of the radius relative to the ulna in the forearm, the *yz*-plane from the forearm coordinate system is used as a neutral plane. A rotation plane is then defined through the radial head center, ulnar fovea, and center of the fossae ridge. The normal of this plane points in the volar direction when the forearm is in the anatomical position. Because the radial–ulnar deviation and flexion–extension of the radius during rotation are minimal, the angle between the planes is considered the position of the radius relative to the ulna. The angle increases when the forearm rotates from supination to pronation.

Table 1 presents all the directions and rotations. The landmarks are visualized in Fig. 2.

### 2.2. Detection of landmarks

The algorithm is separate for the radius and ulna. Both require a 3D bone surface model, or mesh, as input. These can be obtained through CT or MRI by segmentation and surface rendering [2,23]. It is also possible to get a 3D model from orthogonal X-ray images [24].

*Note: the reader is advised to view the supplementary animations in which the algorithms are visualized.*

#### 2.2.1. Detection of radial landmarks

The 3D model of the entire radius is positioned by aligning its principal inertia vectors to the world coordinate system. In this alignment, the world *z*-axis will roughly match with the proximal–distal axis of the bone. To check which side is proximal and distal, 10% of the ends along the *z*-axis of the model are selected, and the volume of their oriented

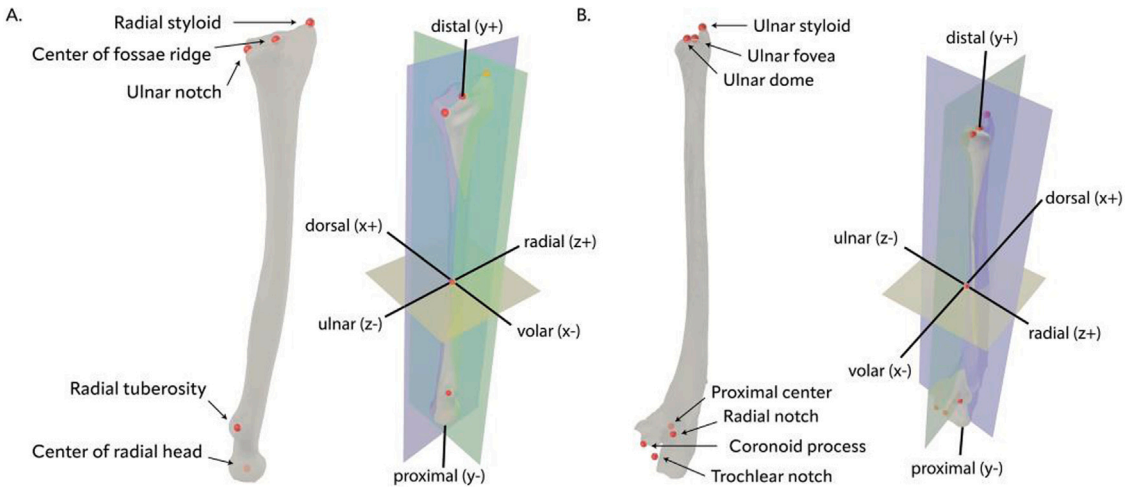


**Fig. 1.** Overview of the radial and ulnar landmarks and coordinate systems. A: the landmarks and coordinate system of the radius. B: the landmarks and coordinate system of the ulna.

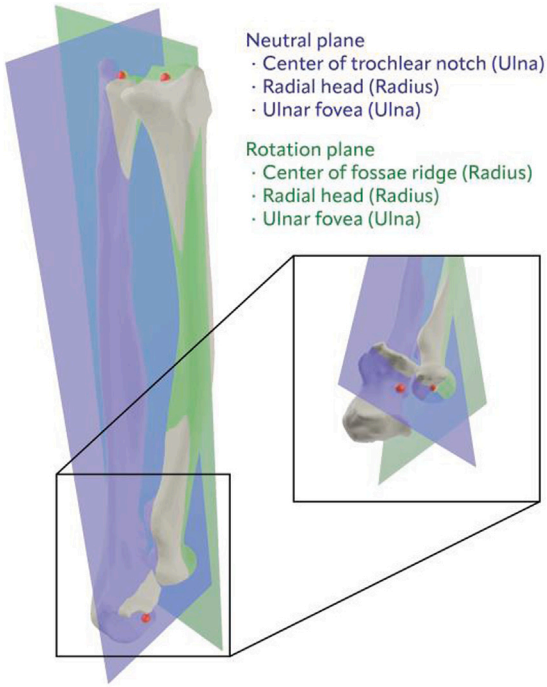


**Fig. 2.** Overview of planes of the forearm used to measure rotational position.

bounding boxes (OBB) are compared. Because the distal radius has a larger volume than the proximal radius, the volume of the OBB at the positive side of the $z$-axis should be the largest.

For the center of the radial head, a plane is fit to the radial joint surface of the humeroradial joint. This is done by selecting the vertices with a $z$-component higher than 0.5 of their vertex normal. The largest connected component with the lowest centroid is selected. The plane that fits on this point cloud is then moved distally until one closed contour is found in the cross section. The intersection of the central axis of the oriented bounding cylinder with the mesh is marked as the center of the radial head.

For the radial tuberosity, cross sections perpendicular to the $z$-axis of the coordinate system will be made at 8% and 20% of its height [25]. A vector from the centroid of the lowest cross section to the center of the highest cross section is calculated and used for new cross sections every millimeter. The areas of all the cross sections are collected, and the sections with a smaller area than the mean are neglected. This selects a part of the model which includes the radial tuberosity. Because of its shape variations, the center of the radial tuberosity is not straightforward [26]. Therefore, regions of 120 degrees around the vector are sliced from the ROI in steps of 10 degrees. The 36 volumes are compared, and the part with the largest volume is considered to be the full radial tuberosity. Its center is determined by casting a ray from the center of the entire diaphyseal part through the center of the radial tuberosity. The location of the intersection is labeled as the radial tuberosity (see Fig. 3).

The radiocarpal joint surface (RCJS) must be isolated for the distal landmarks. Vertices with a $z$-component higher than 0.5 in their vertex normal are selected. The largest connected region of the vertices with the highest centroid is marked as the RCJS. A plane is fit through this point cloud. The plane that fits on this point cloud is then moved proximally until one closed contour is found in the cross-section. From this cross section only the distal geometry is considered. Using its OBB, the long side corresponds to the dorsal and volar sides, and the short side to the radial and ulnar sides. By comparing the mesh inside one-third of the long side of the OBB with their convex hulls, the radial side has the largest difference between the volume of the mesh and its convex hull. This part of the mesh is then rotated in such a way to mimic the 10 degrees volar tilt and 20 degrees radial inclination found in most individuals for the distal radius [27]. The highest point of this transformed mesh is marked as the radial styloid.

The other part of the mesh, the concave part, is split into a volar and dorsal side using a normal vector parallel to the fitted plane, which is perpendicular to the line from the centroid of the mesh to the radial styloid. Cross sections of both parts are made from the radial side to the ulnar side in steps of 1 millimeter. The highest coordinate furthest away from the center is kept for every cross section. This creates a line corresponding to the radiocarpal joint surface's volar and dorsal rim. Both lines are smoothed by fitting a spline with five knots. The points closest to the dorsal line's second knot and the volar line's third knot are connected. The vertex closest to the center of this line is marked as the middle of the fossae ridge. The center of the ulnar notch is found by the intersecting plane through the mean point of the last points of the volar and dorsal rim, the center of the concave mesh, and the center of the fossae ridge. The point closest to the distal bound on the ulnar side is marked as the center of the ulnar notch (see Fig. 4).

### 2.2.2. Detection of ulnar landmarks

The 3D model of the entire ulna is positioned by aligning its principal inertia vectors to the world coordinate system. In this alignment, the world $z$-axis will roughly match with the proximal-distal axis of

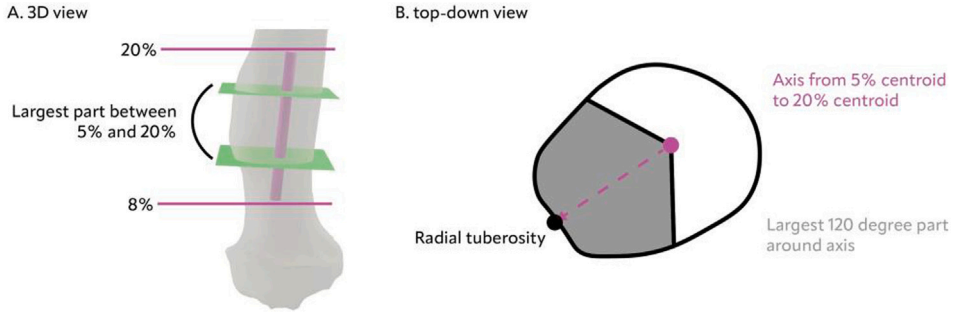


**Fig. 3.** Visualization for finding the radial tuberosity landmark. A: 3D view in which the vector is connected from the 8% to the 20% heights centroid. The cross sections along this axis are kept if their area is larger than the mean. From this volume, parts are sliced 120 degrees around the axis. The part with the largest volume is kept. B: top-down view. Because the tuberosity stands out from the diaphysis of the bone, the central axis does not go through the center of the volume. Because of this offset, a larger volume containing the radial tuberosity can be found.

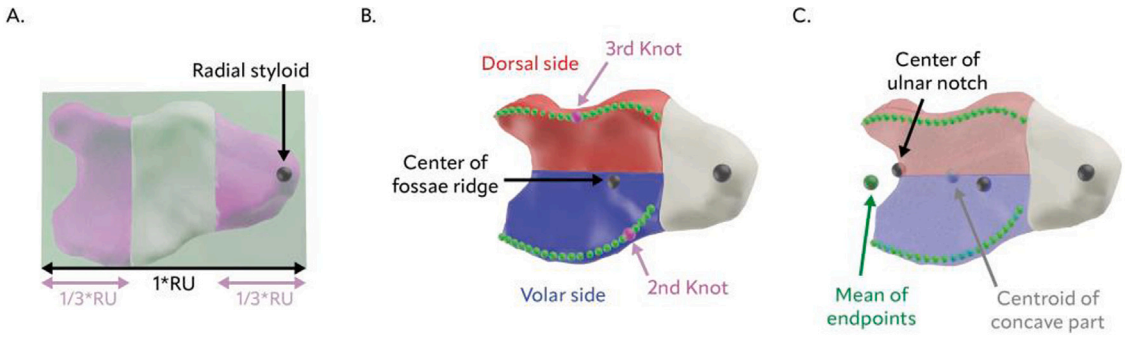


**Fig. 4.** Steps for finding the distal radial landmarks. A: The distal radius's surface is split into three parts using the longest side of the oriented bounding box. The smallest difference between the volume of the mesh and the convex hull is the convex part of the mesh. The highest point is marked as the radial styloid. B: The concave part of the surface is split into a volar and dorsal side. The rims are found using cross sections. After smoothing using splines, the center of the fossae ridge is the mean between the second volar knot and the third dorsal knot. C: A plane through the centroid of the concave part, mean of the endpoints of the rim, fossae ridge center, and the center of the sphere fitted at the ulnar side of the mesh creates a cross section. The most ulnar distal point of the cross section is the center of the ulnar notch.

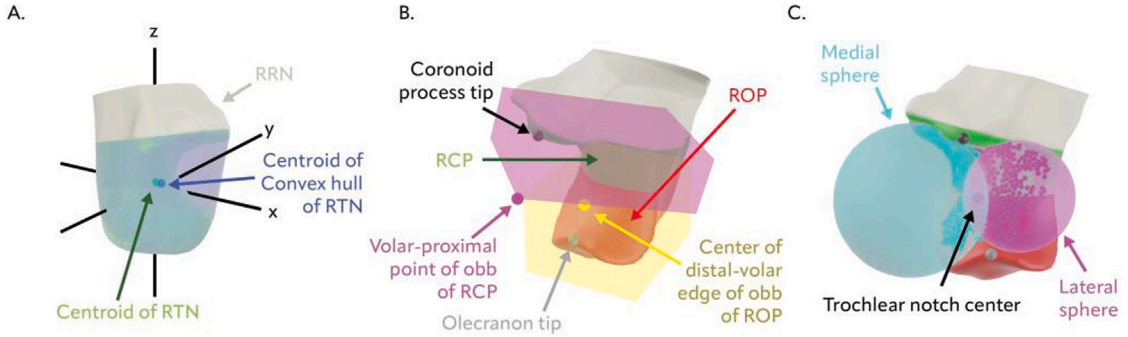


**Fig. 5.** Steps for finding the proximal ulnar landmarks. A: the mesh containing the trochlear notch (RTN) is aligned along the $x$-axis using its centroid and the centroid of its convex hull. The center of the cross section with the largest area is kept in the $xz$-plane. B: The RTN is split at its centroid into a mesh containing the coronoid process (RCP) and a mesh containing the olecranon (ROP). Using their oriented bounding boxes (OBB), the tip of the coronoid process and olecranon can be found. C: a plane through the coronoid process tip, olecranon tip, and the centroids of the RTN, RCP, and ROP splits the RTN into a medial and lateral part. Two spheres can be fit by combining the $x$-values of the vertex normals and their mean curvature. Their radical center is the center of the trochlear notch.

the bone. To check which side is proximal and distal, 15% of the ends along the $z$-axis of the model are selected, and the volume of their OBBs are compared. Because the proximal ulna has a larger volume than the distal ulna, the volume of the OBB at the negative side of the $z$-axis should be the largest.

For the proximal region of interest (PROI), the 20% lowest part of the mesh is selected and its principal inertia vectors are aligned with the world coordinate system without changing the orientation in the proximal-distal axis to correct for the proximal dorsal ulnar angulation [28]. Two regions of interest will be selected: the part of the trochlear notch (RTN) and the part of the radial notch (RRN). Cross sections of the PROI are made with steps of 1 millimeter from proximal to distal. At the height of the cross section with the largest area, the PROI is sliced into a proximal part with the trochlear notch (RTN) and the distal part with the radial notch (RRN) (see Fig. 5).

To identify the RTN's orientation, the mesh's centroid and the centroid of its convex hull are aligned along the world's $x$-axis so that the notch points towards the positive $x$-direction. The RTN is split into a part with the coronoid process (RCP) and a part with the olecranon (ROP) based on the centroid of the RTN. The vertex of the RCP convex hull closest to the most proximal-volar point of its OBB is marked as the tip of the coronoid process. The olecranon tip is the vertex of the ROP convex hull closest to the center of the most volar and distal edge of its OBB.

A plane through the centroid of the RTN, RCP, ROP, tip of the coronoid process, and olecranon is used to divide the RCP into a lateral

and medial part. On both sides, the joint surface of the trochlear notch is restricted by the x-component of the vertex normals on the medial and lateral border. At the same time, the mean curvature determines the proximal and distal border. To improve the curvature of the mesh, this part is smoothed using a dilation and erosion technique [29,30]. Curvature is calculated using the method specified by Cohen-Steiner and Morvan [31]. The radius of the sphere used to calculate the curvature was 0.1 millimeters. By combining vertex normal and curvature information for each vertex, a set of vertices can be selected which represents the joint surface of the trochlear notch on the lateral and medial sides. On both sides, spheres are fit. The trochlear notch center is the radical center of the two spheres.

For locating the radial notch, the vertices on the lateral part of the centroid of the mesh are kept, and their mean curvature is calculated. The mean curvature is thresholded, and the centroid of the largest region is marked as the center of the radial notch. For the proximal center, a cross section is made at the height of the coronoid process. The plane creating the cross section goes through the coronoid process, radial notch, and the cross product of the vectors from the coronoid process to the radial notch and the ulnar dome. The centroid of this cross section is the proximal center.

The distal region of interest (DROI) is defined as the distal 15% of the bounding box along the $z$-axis. Because of differences in anatomy, the angulation and orientation of this part is not equal among individuals [32]. The principal inertia vectors of the DROI are aligned with the world coordinate system without changing the orientation in the proximal-distal axis to correct for this angulation. A plane is moved from distal to proximal along the $z$-axis, and the DROI is cut off when the area of the cross section is smaller than the previous one. Local maxima of the mesh are calculated. In case multiple maxima are found, the maximum with the largest distance to the centroid of the DROI is marked as ulnar styloid.

To find the ulnar fovea and ulnar dome, the ulna's distal tip is rotated so that the vector from the ulnar styloid to the centroid of the mesh is pointing in the positive $x$-direction. The $y$-axis is now equal to the radio-ulnar side. From the volar side, a part of the mesh equal to half of the radio-ulnar length of the bounding box is cut off. This is the ROI for the ulnar dome. The ulnar dome is the intersection of the ray cast from the centroid of the ROI, pointing along the positive $z$-axis. The mesh between the ulnar styloid and the ulnar dome is then cut to define the ROI for the ulnar fovea. Again, the ulnar fovea is the intersection of the ray cast from the centroid of the ROI pointing along the positive $z$-axis (see Fig. 6).

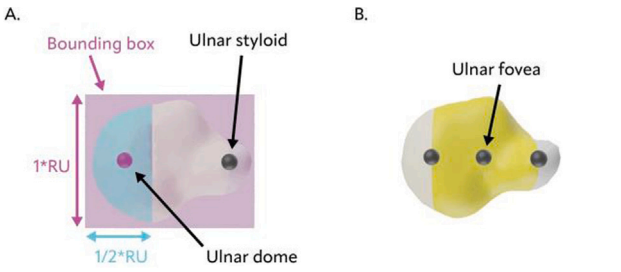


**Fig. 6.** Steps for finding the ulnar dome and ulnar fovea. A: the distal ulnar tip and its bounding box. At the volar side, a part of the mesh is selected, half of the length of the radial–ulnar side of the bounding box. The intersection of a ray from the centroid of this mesh pointing distally is the ulnar dome. B: the mesh between the ulnar dome and ulnar styloid is selected for the ulnar fovea. Again, the intersection of a ray from the centroid of this mesh pointing distally is the ulnar fovea.

## 3. Validation

### 3.1. Experiments

CT scans of 8 forearms from post-mortem human specimens without any apparent deformities or surgical implants were obtained (aged 61–90, 7 right, 1 left, 5 female, 3 male). All humans who donated their bodies for science used in our cadaver study had a written form of consent. No other forms or documentation regarding Dutch law or our institutional ethics committee are necessary. The radius and ulna were segmented, and 3D models were acquired using Materialise Mimics (version 25). Using Materialise MiniMagics software (version 23.5), three researchers with experience in working with 3D models of the forearm manually placed landmarks on the radius and ulna. The five radial landmarks and five of the seven ulnar landmarks were annotated by placing a point on the surface model. The center of the trochlear notch was calculated by the best-fitting circle from three points placed at the narrowest part of the trochlear notch. The researchers did not manually place the proximal point; it is calculated like the automatic method.

For the validation, reference landmarks were calculated using the mean location of all the landmarks placed by the researchers. Left forearms were mirrored to unify the directions in coordinate systems. The radius and ulna were placed separately in the respective coordinate system using the reference landmarks. From this position, the difference between all the automatically placed and manually placed landmarks was calculated in three directions as mentioned in Table 1 and as Euclidean distance (ED). The transformation matrix to transform the radius or ulna with either the manually or automatically placed landmarks to the reference bone is decomposed into Euler angles. The Euler angles are the error for the respective coordinate systems. This is also done for the neutral and rotation planes of the forearm coordinate system. For the position of the radius relative to the ulna, the angle between the normal vectors of the planes is calculated, and the difference between the reference forearm is calculated.

The Wilcoxon rank-sum test is used to compare the automatic errors with the manual errors with the alpha value set at 5%. The decision to use the Wilcoxon rank-sum test is due to the low number of automatic measurements and the errors not following a normal distribution in 16% of the cases. The median, interquartile range (IQR), and full range are given.

### 3.2. Results of the detection of landmarks

Results for the radial landmarks are shown in Table 2. The median error in ED of the radial landmarks for the automated method ranged from 0.4 to 1.1 millimeters. A median error of 1.1 millimeters for ED was seen for the radial tuberosity and the center of the fossae ridge. Both were significantly different from the reference landmarks. The maximum difference in the range for these landmarks is 1.8 and 2.4 millimeters, respectively. When looking into the separate directions, significant differences were seen in three instances: the dorsal-volar direction of the center of the fossae ridge and radial styloid and the distal-proximal direction of the center of the fossae ridge. All of these median differences were less than one millimeter.

Results for the ulnar landmarks are shown in Table 3. The median error in ED of the ulnar landmarks ranged from 0.6 to 1.8 millimeters. A median error of 1.8 millimeters for ED was seen for the proximal center and was significantly different from the reference landmark. This significant difference is also seen in the radioulnar direction of the proximal point. The only other significant difference is seen in the dorsal-volar direction of the trochlear notch. The median difference in both directions is less than one millimeter.

### 3.3. Results of the coordinate system and position calculation

Results for the coordinate systems of the radius, ulna, and forearm, and position calculation can be found in Table 4. The median differences in the radial coordinate system ranged from −0.2 to 0.6 degrees.

**Table 2**
Differences between the radial landmarks of eight specimens detected automatically and manually compared to the mean manual landmarks. For the automated method, eight measurements for each landmark are available; for the manual method, 24 measurements are available.

| Landmark | Dir. | Automatic (mm) | | | Manual (mm) | | | *p*-value |
|---|---|---|---|---|---|---|---|---|
| | | Median | IQR 1–3 | Range | Median | IQR 1–3 | Range | |
| Radial head | DV | −0.2 | −0.5; 0.0 | −0.8; 0.1 | 0.0 | −0.2; 0.2 | −0.6; 0.6 | 0.07 |
| | DP | 0.0 | 0.0; 0.0 | −0.2; 0.0 | 0.0 | 0.0; 0.0 | −0.1; 0.1 | 0.22 |
| | RU | −0.1 | −0.5; 0.1 | −0.8; 0.3 | 0.0 | −0.3; 0.3 | −0.6; 0.7 | 0.30 |
| | ED | 0.4 | 0.3; 0.8 | 0.1; 1.0 | 0.5 | 0.3; 0.6 | 0.0; 0.9 | 0.60 |
| Radial tuberosity | DV | −0.3 | −0.4; 0.1 | −0.8; 0.5 | 0.0 | −0.2; 0.2 | −0.8; 1.0 | 0.32 |
| | DP | 0.2 | −0.3; 0.6 | −1.8; 1.5 | 0.0 | −0.3; 0.3 | −0.8; 0.8 | 0.60 |
| | RU | 0.5 | −0.5; 0.7 | −0.6; 1.0 | 0.2 | −0.4; 0.4 | −1.6; 1.4 | 0.32 |
| | ED | 1.1 | 0.8; 1.5 | 0.8; 1.8 | 0.6 | 0.5; 1.0 | 0.2; 1.9 | 0.02 |
| Ulnar notch | DV | −0.1 | −0.5; 0.1 | −1.0; 0.2 | 0.0 | −0.2; 0.3 | −0.5; 0.4 | 0.24 |
| | DP | 0.1 | −0.2; 0.5 | −0.6; 0.6 | 0.0 | −0.2; 0.1 | −0.4; 0.6 | 0.36 |
| | RU | 0.1 | −0.2; 0.2 | −0.2; 0.5 | 0.0 | −0.1; 0.1 | −0.2; 0.3 | 0.51 |
| | ED | 0.6 | 0.4; 0.8 | 0.3; 1.2 | 0.4 | 0.3; 0.5 | 0.0; 0.7 | 0.06 |
| Fossae ridge | DV | 0.6 | 0.4; 1.0 | −0.1; 1.1 | 0.1 | −0.2; 0.2 | −0.7; 0.9 | <0.01 |
| | DP | 0.3 | 0.2; 0.3 | −0.1; 0.4 | 0.0 | −0.1; 0.1 | −0.5; 0.6 | <0.01 |
| | RU | 0.4 | 0.1; 1.2 | −0.9; 2.2 | 0.0 | −0.3; 0.4 | −0.9; 1.0 | 0.15 |
| | ED | 1.1 | 0.8; 1.4 | 0.4; 2.4 | 0.6 | 0.4; 0.8 | 0.2; 1.4 | 0.01 |
| Radial styloid | DV | −0.3 | −0.9; −0.1 | −1.5; 0.5 | 0.0 | −0.2; 0.1 | −0.7; 0.9 | 0.04 |
| | DP | 0.0 | −0.1; 0.1 | −0.3; 0.2 | 0.0 | 0.0; 0.1 | −0.5; 0.2 | 0.57 |
| | RU | −0.2 | −0.4; 0.1 | −0.6; 0.7 | 0.0 | −0.4; 0.3 | −1.2; 1.3 | 0.57 |
| | ED | 0.6 | 0.4, 1.0 | 0.1; 1.5 | 0.5 | 0.3; 0.7 | 0.0; 1.4 | 0.28 |

Dir: direction; DV: dorsal–volar; DP: distal–proximal; RU: radial–ulnar; ED: euclidean distance.

**Table 3**
Differences between the ulnar landmarks of eight specimen detected automatically and manually compared to the mean manual landmarks. For the automated method, eight measurements for each landmark are available; for the manual method, 24 measurements are available.

| Landmark | Dir. | Automatic (mm) | | | Manual (mm) | | | *p*-value |
|---|---|---|---|---|---|---|---|---|
| | | Median | IQR 1–3 | Range | Median | IQR 1–3 | Range | |
| Trochlear notch | DV | 0.7 | 0.4; 1.2 | −0.1; 2.8 | 0.1 | −0.3; 0.3 | −1.0; 0.8 | <0.01 |
| | DP | 0.1 | −0.4; 0.5 | −0.7; 1.3 | 0.0 | −0.2; 0.2 | −0.5; 0.5 | 0.76 |
| | RU | −0.5 | −0.7; −0.3 | −1.2; −0.1 | 0.1 | −0.7; 0.8 | −1.6; 1.2 | 0.11 |
| | ED | 1.0 | 0.8; 1.9 | 0.6; 3.0 | 0.9 | 0.6; 1.3 | 0.2; 1.7 | 0.30 |
| Coronoid process | DV | 0.1 | −0.1, 0.2 | −0.5; 0.3 | −0.1 | −0.3; 0.3 | −0.8; 1.5 | 0.66 |
| | DP | 0.2 | 0.1; 0.5 | −0.1; 0.8 | −0.2 | −0.3; 0.5 | −0.7; 1.1 | 0.07 |
| | RU | −0.2 | −0.5; 0.1 | −1.8; 1.1 | −0.2 | −0.6; 0.4 | −1.5; 2.4 | 0.54 |
| | ED | 0.7 | 0.4; 0.9 | 0.1; 1.8 | 0.8 | 0.6; 1.2 | 0.2; 2.4 | 0.24 |
| Radial notch | DV | −0.2 | −0.5; 0.0 | −1.0; 1.2 | −0.1 | −0.3; 0.4 | −0.9; 0.9 | 0.46 |
| | DP | 0.3 | 0.1; 0.5 | −0.4; 1.2 | 0.1 | −0.2; 0.3 | −1.2; 1.0 | 0.12 |
| | RU | 0.0 | −0.1; 0.1 | −0.8; 0.8 | −0.1 | −0.2; 0.2 | −0.5; 0.7 | 0.79 |
| | ED | 0.6 | 0.4; 1.0 | 0.3; 1.9 | 0.6 | 0.4; 0.9 | 0.2; 1.2 | 0.76 |
| Proximal center | DV | 0.3 | −0.1; 0.8 | −1.0; 1.9 | 0.0 | −0.1; 0.1 | −0.4; 0.8 | 0.24 |
| | DP | 0.4 | 0.4; 0.5 | −1.0; 0.8 | 0.0 | −0.2; 0.3 | −2.2; 1.7 | 0.08 |
| | RU | 0.8 | 0.2; 1.7 | −1.2; 2.0 | 0.0 | −0.1; 0.1 | −0.4; 0.4 | 0.02 |
| | ED | 1.8 | 1.2; 2.0 | 0.7; 2.2 | 0.4 | 0.3; 0.5 | 0.0; 2.3 | <0.01 |
| Ulnar dome | DV | 0.2 | −0.2; 0.6 | −2.6; 2.0 | 0.2 | −0.7; 0.7 | −2.5; 2.0 | 0.83 |
| | DP | 0.0 | −0.1; 0.1 | −0.7; 0.6 | 0.1 | −0.2; 0.3 | −1.1; 0.5 | 0.76 |
| | RU | 0.3 | 0.1; 0.7 | −0.5; 1.1 | −0.2 | −0.4; 0.4 | −0.8; 0.9 | 0.15 |
| | ED | 1.1 | 0.4; 1.5 | 0.4; 2.7 | 1.0 | 0.6; 1.3 | 0.1; 2.7 | 0.83 |
| Ulnar fovea | DV | −0.4 | −1.0; −0.1 | −2.0; 0.2 | 0.0 | −0.4; 0.3 | −1.0; 1.0 | 0.06 |
| | DP | 0.1 | 0.0; 0.2 | −0.1; 0.9 | 0.0 | −0.1; 0.0 | −0.2; 0.2 | 0.14 |
| | RU | 0.3 | 0.0; 0.5 | −0.2; 0.7 | 0.0 | −0.1; 0.2 | −0.6; 0.4 | 0.05 |
| | ED | 0.6 | 0.4; 1.1 | 0.2; 2.1 | 0.4 | 0.2; 0.7 | 0.0; 1.0 | 0.16 |
| Ulnar styloid | DV | −0.4 | −1.0; 0.2 | −1.2; 0.6 | 0.0 | −0.4; 0.1 | −1.2; 1.2 | 0.32 |
| | DP | 0.0 | 0.0; 0.1 | −0.1; 0.1 | 0.0 | 0.0; 0.0 | −0.2; 0.1 | 0.09 |
| | RU | 0.5 | −0.1; 0.8 | −0.2; 0.9 | 0.0 | 0.0; 0.1 | −0.6; 0.4 | 0.14 |
| | ED | 1.0 | 0.4; 1.2 | 0.2; 1.4 | 0.4 | 0.0; 0.6 | 0.0; 1.3 | 0.05 |

Dir: direction; DV: dorsal–volar; DP: distal–proximal; RU: radial–ulnar; ED: euclidean distance.

The difference in the radio-ulnar direction was significant, with a difference of 0.2 degrees. The median differences in the ulnar coordinate system ranged from −1.4 and 0.1 degrees. None were significant. The median differences in the forearm coordinate system ranged from −0.2 to 2.0 degrees. The difference in the flexion–extension direction of the rotation plane differed significantly, with a difference of −0.2 degrees. The median difference between measuring position automatically and manually is 1.8 degrees.

## 4. Discussion

The results show that our knowledge-based method can localize the important landmarks of the forearm. The median difference is between 0.4 and 1.8 millimeters compared to manually placed landmarks. These errors translate to median angular errors from −1.4 to 2.0, with an error in the position calculation of 1.8 degrees. No difference larger than 4 millimeters was found. The only comparable study for the

**Table 4**
Angular differences between the coordinate systems calculated from the landmarks.

| Coordinate system | Motion | Automatic (°) | | | Manual (°) | | | *p*-value |
|---|---|---|---|---|---|---|---|---|
| | | Median | IQR 1–3 | Range | Median | IQR 1–3 | Range | |
| Radius | FE | −0.2 | −0.3; 0.0 | −0.6; 0.3 | 0.0 | −0.1; 0.1 | −0.4; 0.3 | 0.05 |
| | SP | 0.6 | 0.0; 1.5 | −3.0; 3.5 | 0.0 | −0.5; 0.6 | −1,7; 1.2 | 0.18 |
| | RU | 0.2 | 0.2; 0.3 | 0.0; 0.4 | 0.0 | −0.1; 0.1 | −0.2; 0.3 | <0.01 |
| Ulna | FE | 0.1 | −0.1; 0.4 | −0.4; 0.6 | 0.0 | −0.1; 0.0 | −0.1; 0.2 | 0.41 |
| | SP | −1.4 | −2.0; 3.4 | −6.1; 7.1 | 0.9 | −2.1; 1.9 | −4.6; 4.7 | 1.00 |
| | RU | −0.1 | −0.6; 0.0 | −0.8; −0.1 | 0.0 | −0.1; 0.1 | −0.3; 0.2 | 0.06 |
| Forearm - neutral | FE | −0.2 | −0.4; 0.0 | −0.5; 0.0 | 0.0 | −0.1; 0.1 | −0.3; 0.4 | 0.07 |
| | SP | 2.0 | 0.6; 2.7 | −2.1; 4.7 | −0.4 | −0.8; 1.4 | −2.8; 3.4 | 0.06 |
| | RU | 0.1 | 0.1; 0.2 | −0.3; 0.3 | 0.0 | −0.1; 0.1 | −0.2; 0.2 | 0.06 |
| Forearm - rotation | FE | −0.2 | −0.3; −0.1 | −0.5; 0.1 | 0.0 | −0.1; 0.1 | −0.3; 0.3 | 0.02 |
| | SP | 0.1 | −1.4; 0.6 | −3.8; 2.0 | −0.1 | −0.7; 0.6 | −2.4; 3.5 | 0.73 |
| | RU | 0.1 | 0.0; 0.2 | −0.2; 0.3 | 0.0 | −0.1; 0.1 | −0.3; 0.2 | 0.16 |
| Position | SP | 1.8 | −0.1; 2.9 | −1.1; 7.5 | 0.1 | −1.3; 2.1 | −4.3; 4.9 | 0.10 |

FE: flexion–extension, SP: supination–pronation, RU: radial–ulnar deviation.

upper extremity is from Negrillo-Cardenas et al. [11]. They showed a maximum mean error of 2.4 millimeters for localizing landmarks on the humerus bone, but these measurements were validated against landmarks in phantom bones. In the lower extremity, the femur is often the subject of interest. Negrillio-Cardenas et al. also published a knowledge-based method for the femur, with no mean error larger than 1.7 millimeters [13]. In addition, Subburaj et al. reached an accuracy of 4.9 millimeters for knee landmarks based on surface curvature [6]. For another anatomical region of interest, Fischer et al. used a knowledge-based method to identify pelvic landmarks, which showed a maximum error of 3.3 millimeters and no angular difference larger than 1 degree [10]. The angular differences in our study are larger, especially in the pronation–supination direction, because the distance between the landmarks that define this rotation is minimal. A small change in distance will, therefore, lead to a more considerable angular difference. The same effect can also be seen in the study of Idram et al. which focused on the calcaneus, a relatively small bone [15]. Their root mean squared error was 0.8 millimeters, but also 1.7 degrees.

When using a knowledge-based method, it is essential to see if systemic errors are made in specific directions. For the trochlear notch landmark, this is seen in the dorsal-volar direction: the landmark is almost always placed more dorsally when placed automatically (see Table 3). Because this landmark is used for the neutral plane, this plane is rotated more in pronation (see Table 4). While this difference is not significant and consistently below 2 degrees, it could be explained by how this landmark is placed: automatically, two spheres are fit, while manually, a circle is fit. The same effect of a systemic error can be seen for the localization of the fossae ridge. The automatically placed landmark is often more radial and dorsal, which shows the significant differences in the FE and RU direction of the radial coordinate system. However, the errors are smaller than 0.5 degrees. Depending on the use case, these errors must be considered when using the method. While minor corrections can be introduced to minimize the differences, especially for the SP direction, the lack of a reference standard and the absence of a significant difference due to the comparable spread in manual measurements would first require a validation including a 3D model of the distal humerus to compare the location of the trochlea directly.

As mentioned in the introduction, knowledge-based methods can fail if the landmarks do not follow specific characteristics, as explained in the method. Therefore, the next step for this method would be to test the generalizability of the model in clinical cases. Most forearm fractures are seen in the pediatric population [33]. In this population, joint surfaces are not fully developed yet and could lack essential characteristics [34]. Especially the growth plate in the proximal ulna, which develops into the concave trochlear notch, can only be seen around the age of ten. These variations, which are normal in the pediatric population, can lead to an inadequate performance of the method.

There are two main advantages of this method over manually placing landmarks; the first is the speed. The current implementation of this method in Python showed a maximum time of 15 s for the analysis of the radius and 55 s for the ulna, while manual annotation took several minutes per bone. The difference in time was utterly due to the smoothing step used for the proximal ulna. The Python code, including the smoothing, could have been optimized in terms of time; thus, improvements can still be made. The second advantage is that there is no intra-variability when using an automated method. Because no reference standard is available, the automatic method was compared to the mean of three manual measurements. Calculating an interrater coefficient for the manual measurement based on this reference standard would give biased results. A more robust alternative would be to retrieve a separate set of reference landmarks for all the available forearms. Other studies show good to excellent interrater coefficients [10,12,15]. However, Idram et al. note that some landmarks are hard to recognize and localize within one coordinate. This could be due to unclear anatomy or definition, or the landmark is not merely a point but a larger area, like the center of a notch, depression, or bump, like the radial tuberosity [35]. An automatic method reduces this ambiguity but instead relies on the quality of the 3D model and the accuracy of the segmentation to ensure the correct localization of landmarks. These steps can also be optimized and automated, creating one complete workflow.

Considering the validation and variability, the errors are all below or equal to 2 millimeters and 2 degrees, but there are some significant differences between the automatically and manually placed landmarks. However, some remarks need to be made about the p-values. The low amount of measurements can influence the *p*-value, as significance can be achieved due to a random error. Only eight arms were used, each seen once by three researchers separately. Furthermore, no correction for multiple testing was applied, which could mean that the threshold for significance at 0.05 would be too high. The comparison between the ranges of the automated and manual measurements should be seen in combination with the magnitude of the median error and not by itself.

The next improvement for this method could include a template-based registration beforehand. Fischer et al. have shown that all the landmarks refined using a geometrical approach for the femur showed a smaller error than landmarks without refinement in their study and the study of Baek et al. [12,14]. However, at the moment of writing, no atlas or statistical shape method is available for the whole forearm bones, only for the distal radius [36,37]. While Phan et al. have shown that having one bone as a template could work, the method's applicability increases when the template is based on more bone models, such as pathological and pediatric anatomy, as Schroder et al. proved [16,17].

## 5. Conclusion

Our knowledge-based method is a fast and consistent method for localizing the most important anatomical landmarks on the radius and ulna with all median errors below or equal to 2 millimeters and 2 degrees. Because the use of anatomical landmarks is widespread and the algorithm is relatively simple, our method can be easily implemented, used, and possibly improved by others. Technological improvements follow each other quickly, and obtaining 3D bone models in clinical practice becomes more straightforward. The algorithm has, therefore, the potential to be a fundamental base for the next steps in the 3D analysis of the forearm.

## Compliance with ethical standards

All procedures performed in studies involving human anatomical specimens were in accordance with the ethical standards of the institutional and/or national research committee. All the human anatomical specimens used for our experiments were donated for scientific research and medical training at the Anatomy department of the Erasmus Medical Center and were part of a national body donation program approved by Dutch law and regulations.

## CRediT authorship contribution statement

**Derek F.R. van Loon:** Writing – review & editing, Writing – original draft, Validation, Methodology, Conceptualization. **Eline M. van Es:** Writing – review & editing, Conceptualization. **Denise Eygendaal:** Writing – review & editing, Supervision. **DirkJan H.E.J. Veeger:** Writing – review & editing, Conceptualization. **Joost W. Colaris:** Writing – review & editing, Supervision.

## Declaration of competing interest

The authors declare that they have no known competing financial interests or personal relationships that could have appeared to influence the work reported in this paper.

## Acknowledgments

Special thanks to Frédérique Koopman for placing landmarks. We would like to thank the people who donated their body for science and their relatives at our institution making it possible to perform this study.

## Appendix A. Supplementary data

Supplementary material related to this article can be found online at https://doi.org/10.1016/j.compbiomed.2024.108891.

## References

[1] R.M.Y. Wong, P.Y. Wong, C. Liu, Y.L. Chung, K.C. Wong, C.Y. Tso, S.K.-H. Chow, W.-H. Cheung, P.S.-H. Yung, C.S. Chui, S.W. Law, 3D printing in orthopaedic surgery: A scoping review of randomized controlled trials, Bone Joint Res. 10 (2021) 807–819.

[2] N. Green, V. Glatt, K. Tetsworth, L.J. Wilson, C.A. Grant, A practical guide to image processing in the creation of 3D models for orthopedics, Tech. Orthop. 31 (2016) 153.

[3] A. Mishra, T. Verma, A. Vaish, R. Vaish, R. Vaishya, L. Maini, Virtual preoperative planning and 3D printing are valuable for the management of complex orthopaedic trauma, Chin. J. Traumatol. 22 (2019) 350–355.

[4] C.-T. Ho, H.-H. Lin, E.J.W. Liou, L.-J. Lo, Three-dimensional surgical simulation improves the planning for correction of facial prognathism and asymmetry: A qualitative and quantitative study, Sci. Rep. 7 (2017) 40423.

[5] G. Wu, F.C.T. van der Helm, H.E.J. (DirkJan) Veeger, M. Makhsous, P. Van Roy, C. Anglin, J. Nagels, A.R. Karduna, K. McQuade, X. Wang, F.W. Werner, B. Buchholz, ISB recommendation on definitions of joint coordinate systems of various joints for the reporting of human joint motion—Part II: Shoulder, elbow, wrist and hand, J. Biomech. 38 (2005) 981–992.

[6] K. Subburaj, B. Ravi, M. Agarwal, Automated identification of anatomical landmarks on 3D bone models reconstructed from CT scan images, Comput. Med. Imaging Graph. 33 (2009) 359–368.

[7] M.G.A. de Roo, J.G.G. Dobbe, A. Peymani, A.D. van der Made, S.D. Strackee, G.J. Streekstra, Accuracy of manual and automatic placement of an anatomical coordinate system for the full or partial radius in 3D space, Sci. Rep. 10 (2020) 8114.

[8] S. Poltaretskyi, J. Chaoui, M. Mayya, C. Hamitouche, M.J. Bercik, P. Boileau, G. Walch, Prediction of the pre-morbid 3D anatomy of the proximal humerus based on statistical shape modelling, Bone Joint J. 99-B (2017) 927–933.

[9] N. Xue, M. Doellinger, C.P. Ho, R.K. Surowiec, R. Schwarz, Automatic detection of anatomical landmarks on the knee joint using MRI data, J. Magn. Reson. Imaging 41 (2015) 183–192.

[10] M.C.M. Fischer, F. Krooß, J. Habor, K. Radermacher, A robust method for automatic identification of landmarks on surface models of the pelvis, Sci. Rep. 9 (2019) 13322.

[11] J. Negrillo-Cardenas, J.-R. Jimenez-Perez, H. Canada-Oya, F.R. Feito, A.D. Delgado-Martinez, Automatic detection of landmarks for the analysis of a reduction of supracondylar fractures of the humerus, Med. Image Anal. 64 (2020) 101729.

[12] M.C.M. Fischer, S.A.G.A. Grothues, J. Habor, M. de la Fuente, K. Radermacher, A robust method for automatic identification of femoral landmarks, axes, planes and bone coordinate systems using surface models, Sci. Rep. 10 (2020) 20859.

[13] J. Negrillo-Cardenas, J.-R. Jimenez-Perez, H. Canada-Oya, F.R. Feito, A.D. Delgado-Martinez, Hybrid curvature-geometrical detection of landmarks for the automatic analysis of the reduction of supracondylar fractures of the femur, Comput. Methods Programs Biomed. 226 (2022) 107177.

[14] S.-Y. Baek, J.-H. Wang, I. Song, K. Lee, J. Lee, S. Koo, Automated bone landmarks prediction on the femur using anatomical deformation technique, Comput. Aided Des. 45 (2013) 505–510.

[15] I. Idram, J.-Y. Lai, P.-Y. Lee, A reliable method for morphological measurement of 3D calcaneus models from computed tomography images, Biomed. Res. 30 (2019) 149–159.

[16] C.-B. Phan, S. Koo, Predicting anatomical landmarks and bone morphology of the femur using local region matching, Int. J. Comput. Assist. Radiol. Surg. 10 (2015) 1711–1719.

[17] M. Schröder, H. Gottschling, N. Reimers, M. Hauschild, R. Burgkart, Automated morphometric analysis of the femur on large anatomical databases with highly accurate correspondence detection, Open Med. J. 1 (2014) 15–22.

[18] E. Bermejo, K. Taniguchi, Y. Ogawa, R. Martos, A. Valsecchi, P. Mesejo, O. Ibáñez, K. Imaizumi, Automatic landmark annotation in 3D surface scans of skulls: Methodological proposal and reliability study, Comput. Methods Programs Biomed. 210 (2021) 106380.

[19] J. Montúfar, M. Romero, R.J. Scougall-Vilchis, Hybrid approach for automatic cephalometric landmark annotation on cone-beam computed tomography volumes, Am. J. Orthod. Dentofacial. Orthop. 154 (2018) 140–150.

[20] M. Serafin, B. Baldini, F. Cabitza, G. Carrafiello, G. Baselli, M. Del Fabbro, C. Sforza, A. Caprioglio, G.M. Tartaglia, Accuracy of automated 3D cephalometric landmarks by deep learning algorithms: Systematic review and meta-analysis, Radiol. Medica 128 (2023) 544–555.

[21] Z. Liu, A. Zhou, V. Fauveau, J. Lee, P. Marcadis, Z.A. Fayad, J.J. Chan, J. Gladstone, X. Mei, M. Huang, Deep learning for automated measurement of patellofemoral anatomic landmarks, Bioengineering 10 (2023) 815.

[22] J.G.M. Oonk, J.G.G. Dobbe, G.J. Strijkers, S.K. van Rijn, G.J. Streekstra, Kinematic analysis of forearm rotation using four-dimensional computed tomography, J. Hand Surg. [Eur.] 48 (2023) 466–475.

[23] R.J.A. Kuiper, P.R. Seevinck, M.A. Viergever, H. Weinans, R.J.B. Sakkers, Automatic assessment of lower-limb alignment from computed tomography, J. Bone Joint Surg. 105 (2023) 700.

[24] F. Lebailly, L.V.P.C. Lima, A. Clairemidi, B. Aubert, S. Guerard, Y. Chaibi, J. de Guise, C. Fontaine, W. Skalli, Semi-automated stereoradiographic upper limb 3D reconstructions using a combined parametric and statistical model: A preliminary study, Surg. Radiol. Anat. 34 (2012) 757–765.

[25] C. Gupta, S.G. Kalthur, J.C. Malsawmzuali, A.S. D'souza, A morphological and morphometric study of proximal and distal ends of dry radii with its clinical implications, Biomed. J. 38 (2015) 323–328.

[26] A.D. Mazzocca, M. Cohen, E. Berkson, G. Nicholson, B.C. Carofino, R. Arciero, A.A. Romeo, The anatomy of the bicipital tuberosity and distal biceps tendon, J. Shoulder Elb. Surg. 16 (2007) 122–127.

[27] P. Hosseinzadeh, D. Olson, R. Eads, A. Jaglowicz, C.A. Goldfarb, S.A. Riley, Radiologic evaluation of the distal radius indices in early and late childhood, Iowa Orthop. J. 38 (2018) 137–140.

[28] M. Mostowy, J. Paul, A. Majos, C. Mefleh, M. Piwnik, P. Kowalski, S. Kobielski, S. Choate, D. Buzas, A. Kwapisz, Proximal ulna morphology in various pediatric population age groups: Proximal ulna dorsal angulation (PUDA) and olecranon tip-to-apex (TTA) distance, Surg. Radiol. Anat. 45 (2023) 893–899.

[29] A. Bacciaglia, A. Ceruti, A. Liverani, Surface smoothing for topological optimized 3D models, Struct. Multidiscip. Optim. 64 (2021) 3453–3472.

[30] S. Sellán, J. Kesten, A.Y. Sheng, A. Jacobsen, Opening and closing surfaces, ACM Trans. Graph. 39 (2020) 1–13.

[31] D. Cohen-Steiner, J.-M. Morvan, Restricted delaunay triangulations and normal cycle, in: Proceedings of the Nineteenth Annual Symposium on Computational Geometry, Association for Computing Machinery, ISBN: 978-1-58113-663-0, 2003, pp. 312–321.
[32] P. Daneshvar, R. Willing, M. Lapner, M.A. Pahuta, G.J.W. King, Rotational anatomy of the radius and ulna: Surgical implications, J. Hand Surg. 45 (2020) 1082.e1–1082.e9.
[33] L. Rennie, C.M. Court-Brown, J.Y.Q. Mok, T.F. Beattie, The epidemiology of fractures in children, Injury 38 (2007) 913–922.
[34] A. Dimeglio, Growth in pediatric orthopaedics, J. Pediatr. Orthop. 21 (2001) 549.
[35] W. Schlicher, I. Nielsen, J.C. Huang, K. Maki, D.C. Hatcher, A.J. Miller, Consistency and precision of landmark identification in three-dimensional cone beam computed tomography scans, Eur. J. Orthod. 34 (2012) 263–275.
[36] A. Peymani, I. Dobbe, S. van Rijn, H. McCarroll, G. Streekstra, S. Strackee, P141. A 3D statistical shape model of the distal radius in madelung deformity, Plast. Reconstr. Surg. Global Open 10 (2022) 116–117.
[37] S.F. Baumbach, J. Binder, A. Synek, F.G. Mück, Y. Chevalier, E. Euler, G. Langs, L. Fischer, Analysis of the three-dimensional anatomical variance of the distal radius using 3D shape models, BMC Med. Imaging 17 (2017) 23.